

Properties of a solar flare kernel observed by Hinode and SDO

P. R. Young¹, G. A. Doschek², H. P. Warren²

and

H. Hara³

ABSTRACT

Flare kernels are compact features located in the solar chromosphere that are the sites of rapid heating and plasma upflow during the rise phase of flares. An example is presented from a M1.1 class flare observed on 2011 February 16 07:44 UT for which the location of the upflow region seen by EIS can be precisely aligned to high spatial resolution images obtained by the Atmospheric Imaging Assembly (AIA) and Heliospheric Magnetic Imager (HMI) on board the Solar Dynamics Observatory (SDO). A string of bright flare kernels is found to be aligned with a ridge of strong magnetic field, and one kernel site is highlighted for which an upflow speed of $\approx 400 \text{ km s}^{-1}$ is measured in lines formed at 10–30 MK. The line-of-sight magnetic field strength at this location is $\approx 1000 \text{ G}$. Emission over a continuous range of temperatures down to the chromosphere is found, and the kernels have a similar morphology at all temperatures and are spatially coincident with sizes at the resolution limit of the AIA instrument ($\lesssim 400 \text{ km}$). For temperatures of 0.3–3.0 MK the EIS emission lines show multiple velocity components, with the dominant component becoming more blue-shifted with temperature from a redshift of 35 km s^{-1} at 0.3 MK to a blueshift of 60 km s^{-1} at 3.0 MK. Emission lines from 1.5–3.0 MK show a weak redshifted component at around $60\text{--}70 \text{ km s}^{-1}$ implying multi-directional flows at the kernel site. Significant non-thermal broadening corresponding to velocities of $\approx 120 \text{ km s}^{-1}$ is found at 10–30 MK, and the electron density in the kernel, measured at 2 MK, is $3.4 \times 10^{10} \text{ cm}^{-3}$. Finally, the Fe XXIV $\lambda 192.03/\lambda 255.11$ ratio suggests that the EIS calibration has changed since launch, with the long wavelength channel less sensitive than the short wavelength channel by around a factor two.

Subject headings: Sun: flares — Sun: activity — Sun: corona — Sun: UV radiation — Sun: transition region — Sun: chromosphere

¹College of Science, George Mason University, 4400 University Drive, Fairfax, VA 22030

²Naval Research Laboratory, 4555 Overlook Avenue SW, Washington DC 20375

³National Astronomical Observatory of Japan/NINS, 2-21-1 Osawa, Mitaka, Tokyo 181-8588, Japan

1. Introduction

Early spectroscopic measurements of emission lines formed at ~ 10 MK obtained during the rise phase of solar flares revealed blue-shifted components corresponding to plasma upflows of several hundred km s^{-1} (Doschek et al. 1980; Antonucci et al. 1982). Theoretical models of 1D solar loops in which energy is deposited near the loop top demonstrated that such large upflows could be generated as low-lying chromospheric plasma is heated to coronal temperatures and “evaporates” into the coronal part of the loop (Cheng et al. 1983). The plasma upflow sites have also been correlated with brightenings in the chromosphere (Mason et al. 1986), transition region and corona (Del Zanna et al. 2006). In the present work we define intense brightenings that occur during the flare rise phase as *flare kernels*. It is not known if flare kernels always exhibit fast upflows in ~ 10 MK emission lines but the many reported measurements of hot, blue-shifted emission lines in X-ray and ultraviolet spectra suggests that this is possible.

The availability since 2010 of high spatial and time resolution EUV images from the Atmospheric Imaging Assembly (AIA) on board the Solar Dynamics Observatory (SDO), coupled with high resolution EUV spectra from the EUV Imaging Spectrometer (EIS) on board *Hinode* gives an unprecedented capability for studying flare kernels. The present work focusses on one particular kernel observed by both instruments on 2011 February 16 during the rise phase of a M1 class flare.

Flare kernels can be interpreted in terms of the Standard Flare Model (see Benz 2008, and references therein), which posits an energy release site in the corona that leads to either a stream of non-thermal particles or a thermal conduction front being directed down the coronal loop legs towards the photosphere. Heating then occurs in the chromosphere leading to flare ribbons and brightenings, and hot plasma rises towards the flare site, giving bright post-flare loops. The flare kernels are then the sites of chromospheric heating, and would be expected to be bright in emission lines formed at all temperatures from the chromosphere to ~ 10 MK. In addition, large plasma flows would be expected as heated plasma rises into the corona. The case for which non-thermal particles heat the chromosphere has been investigated theoretically, and two evaporation scenarios identified: for low particle fluxes ($< 3 \times 10^{10} \text{ erg cm}^{-2} \text{ s}^{-1}$) “gentle” evaporation occurs with speeds up to 30 km s^{-1} ; while for high particle fluxes “explosive” evaporation occurs with speeds of several hundred km s^{-1} in the corona (Fisher et al. 1985). Evidence for both evaporation scenarios has been found (e.g., Milligan et al. 2006b; Teriaca et al. 2003) and, further, evidence for the momentum of hot upflowing plasma balancing the momentum of cool, downflowing plasma during explosive evaporation is indicated in some events (Teriaca et al. 2006).

The detection of blueshifted emission components of hot lines was initially confined to spatially-unresolved X-ray spectra (Doschek et al. 1980; Antonucci et al. 1982), which always showed a dominant emission component near the rest wavelength of the line with the high velocity component present as a weaker shoulder on the short wavelength side. The dominant, at-rest emission component can not be explained by chromospheric evaporation models unless an ensemble of many events occurring at different times is assumed (Cheng et al. 1983; Hori et al. 1997, 1998;

Warren & Doschek 2005). Spatially resolved spectra would be expected to resolve flare kernels and thus reveal a dominant, highly-blueshifted plasma component but a detailed study had to await the launch of the Coronal Diagnostic Spectrometer (CDS) on board the Solar and Heliospheric Observatory (SOHO) in 1995. CDS observed the Fe XIX $\lambda 592.2$ line, formed at 9 MK, with a spatial resolution of around $6-8''$. Many papers reported blueshifts of the Fe XIX line, with upflow speeds of up to 230 km s^{-1} (Brosius 2003; Brosius & Phillips 2004; Harra et al. 2005; Milligan et al. 2006a,b; Del Zanna et al. 2006). The fairly low spectral resolution of CDS meant that multi-component fitting of the Fe XIX line was generally not possible, although Teriaca et al. (2003), Milligan et al. (2006a) and Teriaca et al. (2006) reported observations for which two components could be fit. For the latter two papers the high velocity component was dominant and the blueshifted components implied upflow speeds of 230 and 200 km s^{-1} . These results were the first instances whereby a dominant upflow component was measured during the impulsive phase of a flare, suggesting that the evaporation site had been resolved. We note that the upflow velocities are somewhat smaller than the values derived by multiple component fitting of spatially unresolved X-ray data for which values of around 400 km s^{-1} could be measured (Antonucci et al. 1982; Fludra et al. 1989). This may reflect the lower temperature of formation of the Fe XIX line compared to the X-ray lines.

The EIS instrument presents a significant improvement in both spatial and spectral resolution over CDS, and it also has access to hotter emission lines from Fe XXIII and Fe XXIV, formed in the range 10–30 MK. The first study of the impulsive phase of a flare observed by EIS was performed by Milligan & Dennis (2009), who presented Doppler measurements at the footpoints of a C1.1 flare. Emission lines formed below 5 MK were found to have Gaussian profiles, and Doppler shifts showed a change from redshifts to blueshifts at around 2 MK. This was cited as evidence of explosive evaporation, whereby cooler plasma recoils towards the photosphere and hotter plasma rises upwards towards the corona. Lines from the hottest species, Fe XXIII and Fe XXIV (10–30 MK), showed two emission components, the dominant being close to the rest wavelengths of the lines, the weaker at velocities of $< -200 \text{ km s}^{-1}$. This is similar to the earlier X-ray observations, a surprise given that the footpoints are resolved by EIS.

The most relevant study for the present work is that of Watanabe et al. (2010) who presented observations of a C9.7 confined flare. The region displayed four intense brightenings during the flare rise phase that were interpreted as loop footpoints. Three spectra of Fe XXIII $\lambda 263.77$ (formed at 15 MK) obtained of one of the footpoints during the rise phase and separated by 160 s show (1) a small blueshift of -55 km s^{-1} , (2) a two component profile with a dominant component at a velocity of at least -382 km s^{-1} , and (3) a single component profile at a velocity of -40 km s^{-1} . For spectrum 2, the Fe XVI $\lambda 262.99$ line (3 MK) showed a two component profile with the weaker blueshifted component at -116 km s^{-1} . All cooler lines do not show evidence of a blueshifted component in any of the spectra. The dominant high velocity Fe XXIII upflow found in spectrum 2 is similar to that found from CDS data by Milligan et al. (2006a) and Teriaca et al. (2006) only that the magnitude of the velocity is significantly larger. We note that the properties derived from spectrum 2 of Watanabe et al. (2010) are quite similar to those found in the present work.

The impulsive phase of a smaller B2 class flare was studied by Del Zanna et al. (2011) and a key result was the finding of blue-shifted components of Fe XIV, XV and XVI lines (2–3 MK) with velocities of 40–60 km s^{−1}. The rest components of the lines were stronger in intensity. The Fe XXIII and Fe XXIV lines were weak in this flare, and velocity results were not discussed.

Graham et al. (2011) presented observations of a C7 flare and found a blue wing enhancement to the Fe XVI λ 262.98 emission line (formed at 2.5 MK), corresponding to upflow velocities of up to 140 km s^{−1}. As noted above, a blue-shifted component for Fe XVI was found by Watanabe et al. (2010) and Del Zanna et al. (2011), and is also found in the present work. Graham et al. (2011) did not find any high velocity components for other lines, and Doppler shifts were generally in the −20 to 0 km s^{−1} range.

The first EIS observation of a flare with a sit-and-stare study was recently reported by Brosius (2013) for a C1 flare. Although the slit position did not lie directly on the flare loop footpoint, line-of-sight velocities measured in the leg of the loop from Fe XXIII gave a peak velocity of −208 km s^{−1}. Note that the emission line was completely blueshifted for 156 s, and then displayed a two component profile with a dominant stationary component and weak blueshifted component for a further 56 s.

Doschek et al. (2012) studied a M1.8 class flare observed by EIS in 2012 March, and a spectrum obtained during the rise phase did not reveal any significant Doppler flows in Fe XXIII λ 263.77 (formed at 15 MK), however emission lines of Fe XIII and Fe XIV (formed at 2 MK) showed extended short wavelength wings that are due to downflowing plasma. Similar profiles are found in the present work for Fe XIV. Doppler shifts of ≈ -100 km s^{−1} for Fe XXIII are found at a later phase of the flare by Doschek et al. (2012) suggesting the presence of hot, evaporating plasma.

The new aspect of the present work is the ability to accurately co-align the EIS data with high spatial and temporal images from the AIA instrument, allowing the flare evaporation site to be studied in great detail. Our analysis begins with a summary of the data-sets used (Sect. 2) and an overview of the active region and flare (Sect. 3). Sect. 4 presents the analysis of the EIS flare kernel spectrum, and Sects. 5 and 6 present analysis of the imaging data-sets from SDO and *Hinode*. Results are summarized in Sect. 7.

2. Dataset overview

The data analyzed in the present work principally come from the EUV Imaging Spectrometer (EIS; Culhane et al. 2007) on board the *Hinode* satellite, and the Atmospheric Imaging Assembly (AIA; Lemen et al. 2012) on the Solar Dynamics Observatory (SDO). Additional data come from the Helioseismic and Magnetic Imager (HMI; Scherrer et al. 2012) on board SDO and the *Hinode*/X-Ray Telescope (XRT; Golub et al. 2007). Unfortunately the Reuven Ramaty High Energy Solar Spectroscopic Imager (RHESSI) was in spacecraft night during the rise phase of the flare and so no data were available.

Much of the data calibration and analysis performed for the present work made use of IDL software routines that are part of the *Solarsoft* distribution. AIA data downloaded from the Joint Science Operations Center (JSOC) or the Virtual Solar Observatory (VSO) are provided in level-1 format which means that they have been flat-fielded, de-spiked and calibrated. The AIA data shown in this work were “re-spiked” using the IDL routine `AIA_RESPIKE` as it was found that some of the flare kernels were incorrectly flagged by the AIA de-spiking routine. The files were then processed with `AIA_PREP` to convert them to level-1.5 format, which places all of the different AIA filter images onto the same plate scale. The HMI data were also processed with `AIA_PREP` to place them on the same plate scale as the AIA images.

The AIA detectors register events in “data numbers” (DN) such that DN values between 0 and $2^{14} - 1$ ($=16,383$) can be measured in a single exposure. During flares the maximum value can be reached, leading to saturation, and the extent of saturation varies depending on the sensitivity of the different AIA channels and the strength of the radiation that the channels measure. Usually fixed exposure times for the AIA channels are used, but during flares the exposure times can be automatically reduced to help prevent saturation. For the present observation, however, most of the AIA channels were badly affected by saturation during the flare, with the 94 Å channel the only one completely unaffected. (Note that in flare conditions this channel is dominated by Fe XVIII $\lambda 93.93$, formed at 7 MK.)

AIA obtains full-disk images at a 12 s cadence in seven different EUV filters, and at a 24 s cadence in two UV filters. The filters are identified by the wavelength of peak sensitivity, and we use the shorthand A94, A131, etc., to refer to the filters with wavelengths 94 Å, 131 Å, etc. The pixel size of the images corresponds to an angular area of 0.6×0.6 arcsec² on the Sun.

EIS spectroscopic observations are obtained by scanning a narrow slit over an area of the Sun. At each pixel position along the slit, spectra covering the ranges 170–212 Å and 246–292 Å are obtained, however due to telemetry restrictions only narrow wavelength windows centered on specific emission lines are usually downloaded. On 2011 February 16 EIS continuously ran a single observation study called `HH_Flare_180x160_v2` for the period 06:17–12:23 UT, yielding 64 rasters in all. For each raster the 2'' slit scanned an area of 180×160 arcsec² in 5 min 45 s. An 8 s exposure time was used and the slit jumped 5'' between exposure positions. Ten wavelength windows are obtained with the `HH_Flare_180x160_v2` study, and the particular emission lines studied in the present work are listed in Table 1.

The EIS data were calibrated with the `EIS_PREP` routine in *Solarsoft* using the standard processing options listed on the EIS wiki¹, and “missing” data (due to warm pixels, cosmic rays, etc.) were interpolated using the procedure described in Young (2010). The `/CORRECT_SENSITIVITY` keyword was used, which implements a wavelength-independent sensitivity decay for the instrument with an e-folding time of 1894 days, which means that the line intensities tabulated in the present

¹<http://msslxr.mssl.ucl.ac.uk:8080/eiswiki/>

work are a factor 2.3 higher than if the pre-launch calibration had been used. At the time of writing the EIS calibration is under revision by the EIS team, and it seems likely that some wavelength regions have decayed less strongly than suggested by the earlier analysis. If correct, then this would lower the intensities given in the present work.

Given the high time cadence of the instruments used for this work, it is important to state observation times precisely. When times of individual exposures of AIA, HMI and EIS are referred to, the time corresponds to the midpoint of the exposure given in Coordinated Universal Time (UTC). For the SDO instruments, this is the parameter `T_OBS` stored in the data header, although for HMI this value has to be converted from International Atomic Time to UTC. For EIS the midpoint of an exposure is defined as the time midway between the shutter open and close times, which are stored in the EIS data file headers.

3. Overview of active region of AR 11458

Active region AR 11458 was the first major flaring active region of solar cycle 24 and so many aspects of the region’s flares and magnetic evolution have already been studied. The dominant flaring activity took place during 2011 February 13–18, with the largest event an X2.2 class flare on February 15 that produced a sunquake (Kosovichev 2011) and Earth-directed coronal mass ejection (CME; Schrijver et al. 2011). A M1.6 flare on February 16 also produced a CME that has been spectroscopically studied with the EIS instrument (Harra et al. 2011; Veronig et al. 2011).

Prior to 15 UT on February 15 the flares from AR 11458 were generally eruptive events with significant jetting and CME activity. From 15 UT up to the M1.6 flare at 14:25 UT on February 16, however, the five C5 or greater flares that took place were all confined flares. For this work we focus on the fourth flare in this sequence: a M1.1 class flare that peaked in the GOES 1–8 Å X-ray light curve at 07:44 UT on February 16. This flare was chosen as the EIS observation revealed the location of a high velocity upflow at temperatures of 10–30 MK during the flare rise phase. Such locations are often missed by EIS raster scans as they have short lifetimes and they occur in only specific parts of the active region. The topology of the active region and post-flare loops also gives a relatively clean view of the upflow site, with a clear correlation with intense, compact brightenings in AIA images. The EIS spectroscopic properties of the upflow site are similar to those measured by Watanabe et al. (2010) from a C9.7 flare observed in 2007, but the availability of SDO data gives a greater insight into the properties of the flare upflow region.

Figure 1 shows before-and-after images of AR 11458 obtained with the AIA 193 Å filter, which demonstrate that the peripheral loop structures remain largely unchanged following the flare. The HMI LOS magnetogram and continuum images in Figure 1 show the photospheric structure of the active region prior to the flare.

The flare emission is best seen in the AIA 94 Å filter images and Figure 2 shows two images, one from the rise phase (a) and one taken a few minutes after the flare peak (b). The image times

are indicated on the GOES X-ray light curve (Figure 2c). During the rise phase, flare kernels are seen at three locations in the active region that approximately correspond to the footpoints of the post-flare loops that eventually appear. The most intense flare loops connect the two central sunspots (see also Figure 1), while another fainter, more twisted set of loops connects the central, positive polarity sunspot to the negative polarity sunspot at the east side of the active region (Figure 2b).

4. EIS data analysis

The group of A94 flare kernels highlighted in Figure 2a were scanned by EIS with a raster that began at 07:38:26 UT and finished at 07:44:22 UT (note that EIS rasters west-to-east). Five consecutive raster positions obtained between 07:40:16 UT and 07:40:51 UT revealed five intense, compact brightenings in most of the EIS lines (Figure 3). The hot Fe XXIII $\lambda 263.77$ line (formed at 15 MK) does not show the brightenings as a short, intense post flare loop dominates the image. However an image formed in the short wavelength wing of the line at around -350 km s^{-1} does show the brightenings (lower-right panel of Figure 3). For this work we focus on the right-most of the five brightenings, which was observed by EIS at 07:40:16 UT.

Figure 4 shows intensity cross-sections through the selected brightening in the solar-Y direction (i.e., along the EIS slit). Each intensity cross-section is co-spatial in the X-direction and co-temporal by the nature of spectrometer observations. The cross-sections have been aligned with each other by making use of the known spatial offsets in the solar-Y direction (due to grating tilt and CCD spatial offsets) that are obtained from the IDL routine `EIS_CCD_OFFSET`.

A striking feature of the brightening is that the intensity peaks at the same pixel for all temperatures from 0.3 MK (O VI) to 20 MK (Fe XXIV). The intensity profiles are also very similar: Gaussian shapes with a full-width at half-maximum of about 4 pixels. (The Fe XVI profile is affected by significant background coronal emission.) The EIS spatial resolution has been independently estimated as 3–4'' based on comparisons with AIA images and studies of transition region brightenings², suggesting the observed feature is not resolved by EIS. This is confirmed by the higher spatial resolution images from AIA (Sect. 5).

At the location of the brightening it is found that Fe XXIV $\lambda 192.03$ has a strong emission component at a velocity of $\approx -400 \text{ km s}^{-1}$ – see discussion later. The intensity cross-section for this blue component is also shown in Figure 4 and is consistent with the others.

The presence of plasma with a wide range of temperatures compacted into a single bright feature is expected for the standard model of chromospheric evaporation whereby chromospheric plasma at the footpoint of the flare loop is rapidly heated to multi-million degree temperatures.

²See discussion at <http://msslxr.mssl.ucl.ac.uk:8080/eiswiki>.

Further support comes from the presence of rapidly upflowing plasma at the hottest temperatures, however the finding of multiple velocity components in the emission lines is not compatible with a simple, single loop model and suggests further complexity.

In the following sections we study the spectroscopic properties of the brightening in more detail. To do this we create a single spectrum for the brightening in order to measure line intensities, widths and Doppler shifts. The process is complicated however by the fact that the background coronal emission is significant for some of the emission lines. Sect 4.1 describes how the background emission is dealt with and how the spectrum is extracted. Sect. 4.2 discusses blending issues for the emission lines, and Sects. 4.3–4.6 present the results for Doppler shifts, line widths, emission measure and density.

4.1. Extracting the spectrum of the flare kernel

As discussed in the previous section, EIS does not spatially resolve the flare kernel site and so we assume that the Gaussian-shaped intensity profiles shown in Figure 4 all come from a single, unresolved structure. Practically this means that we sum the intensity from 9 Y-pixels distributed over the intensity cross-sections to yield a single spectrum for the flare kernel. However, Figure 4 shows that there is background emission against which the kernel appears in all of the EIS lines. This background emission is particularly significant for Fe XV and Fe XVI. In addition to affecting the intensity of the emission lines, we also find that this emission distorts the emission line profiles, which then affects the measurement of line widths and velocities. For this reason we subtract a pre-flare spectrum from the flare kernel spectrum.

The pre-flare spectrum was obtained from the previous EIS raster, which began at 07:32 UT. This raster showed much reduced emission at the positions of the five flare kernels and so we can consider it to give a good representation of the pre-flare corona at the locations of the brightenings.

The background corona subtraction is performed with the *Solarsoft* routine EIS_MASK_SPECTRUM, which performs the procedure as follows. Each spectral window from an EIS raster yields a 3D intensity array of wavelength, solar-X and solar-Y pixels. Since the satellite pointing does not change between the pre-flare and flare rasters, then potentially one can simply take the spatial pixels corresponding to the brightening and subtract the pre-flare spectra from the flare spectra. The situation is complicated, however, by the fact that the EIS wavelength scale drifts with time due to the thermally-induced motion of the EIS grating during an orbit (referred to as spectrum drift). Therefore in order to perform the pre-flare spectrum subtraction, it is necessary to place the spectra at each spatial pixel in each raster onto a common wavelength scale. This is done with the IDL routine EIS_SHIFT_SPEC, which shifts the spectra for each spatial pixel of a raster onto a common wavelength scale by making use of the spectrum drift and slit tilt corrections of Kamio et al. (2010). The pre-flare spectrum can then be subtracted from the flare spectrum at each spatial pixel. The background-subtracted spectra from the 9 Y-pixels that span the flare kernel are

Table 1. EIS emission line parameters.

Ion	Wavelength	$\text{Log } T_{\text{mem}}$	Component	Intensity ($\text{erg cm}^{-2} \text{ s}^{-1} \text{ sr}^{-1}$)	LOS velocity (km s^{-1})	Non-thermal velocity (km s^{-1})	Log_{10} (Column emission measure / cm^{-5})
O VI	$\lambda 184.12$	5.51	1	43751 ± 921	34.5 ± 3.8	60.0 ± 3.5	29.91
Fe X	$\lambda 184.54$	6.05	1	82385 ± 1382	17.4 ± 3.8	81.5 ± 3.4	29.65
Fe XII	$\lambda 192.39$	6.20	1	24687 ± 565	-19.5 ± 2.0	18.6 ± 3.2	29.46
			2	9445 ± 697	73.7 ± 3.7	18.6 ± 3.2	29.04
Fe XIV	$\lambda 264.79$	6.30	1	82449 ± 882	-31.0 ± 1.2	28.1 ± 2.1	29.61
			2	21558 ± 878	64.9 ± 2.8	28.1 ± 2.1	29.03
Fe XIV	$\lambda 274.20$	6.30	1	33731 ± 599	-33.0 ± 1.3	32.1 ± 2.2	29.60
			2	10653 ± 567	69.0 ± 3.0	32.1 ± 2.2	29.10
Fe XV	$\lambda 284.16$	6.34	1	18971 ± 1530	-149.8 ± 3.7	29.8 ± 2.0	28.29
			2	320560 ± 3060	-48.3 ± 0.6	29.7 ± 2.0	29.52
			3	40236 ± 1310	79.9 ± 1.6	29.7 ± 2.0	28.62
Fe XVI	$\lambda 262.98$	6.43	1	972 ± 297	-249.0 ± 18.4	20.4 ± 3.0	28.22
			2	6398 ± 1045	-145.6 ± 8.2	20.4 ± 3.0	29.04
			3	31990 ± 1188	-59.9 ± 2.2	20.3 ± 3.0	29.74
			4	1381 ± 334	79.0 ± 12.4	20.3 ± 3.0	28.38
Fe XXIII	$\lambda 263.77$	7.16	1	10584 ± 470	-384.7 ± 3.8	120.6 ± 6.6	30.15
			2	3985 ± 382	24.0 ± 8.1	111.6 ± 13.3	29.73
Fe XXIV	$\lambda 192.03$	7.25	1	102900 ± 685	-404.8 ± 1.3	113.3 ± 3.0	29.89
			2	42488 ± 599	5.3 ± 1.7	127.1 ± 3.6	29.51
Fe XXIV	$\lambda 255.11$	7.25	1	26762 ± 1172	-425.1 ± 2.6	85.3 ± 5.7	29.70
			2	6856 ± 738	-4.6 ± 4.6	34.8 ± 10.3	29.11

then summed to yield the final spectrum.

Figure 5 shows how the subtracted spectrum (blue) compares with the un-subtracted spectrum (black) and the pre-flare spectrum (red) for four emission lines. For Fe XV $\lambda 284.16$ and Fe XVI $\lambda 262.98$ it is clear that the pre-flare emission lines, which are close to at rest, when subtracted result in the centroid being pushed to shorter wavelengths. The method for setting the rest wavelength for these spectra is discussed in Sect. 4.3.

A key uncertainty in the background subtraction method is the EIS pointing stability: if the pointing changed between the 07:32 and 07:38 UT rasters, then the pre-flare background at the site of the brightening is no longer valid. The *Hinode* pointing is known to exhibit peak-to-peak pointing fluctuations of up to $3''$ in both X and Y directions (Mariska & Muglach 2010), but a benefit for the present analysis is that *Hinode* was pointed at AR 11458 for long periods of time, meaning that the satellite and the instruments received a nearly fixed illumination from the Sun (re-pointing of the satellite leads to varying illumination and thus thermal effects). The IDL routine EIS_JITTER returns estimates of the instrument pointing jitter, and this shows variations of $\leq 0.25''$ in solar-X and $\leq 1.2''$ in solar-Y. For the solar-Y direction, pointing can be checked by comparing intensity cross-sections and it can be seen that features in solar-Y away from the flare site are well-matched to within a pixel between the 07:32 and 07:38 UT rasters. We thus believe our background subtraction method is not significantly affected by pointing jitter.

4.2. Line fitting notes

The spectrum extraction method described above yields a single EIS spectrum for the flare kernel. The emission lines were fit with Gaussian functions using the IDL routine SPEC_GAUSS_EIS. Most of the lines have non-Gaussian shapes, suggesting the presence of multiple plasma components at different velocities and specific details on how each emission line was treated are given below. The line fit parameters, expressed as intensity, line-of-sight (LOS) velocity and non-thermal broadening, are given in Table 1. From the line intensity the column emission measure can be derived, and this quantity is also shown in Table 1. The temperature of maximum emission, T_{mem} , given in Table 1 is the temperature at which a line’s contribution function peaks and is derived using version 7.1 of the CHIANTI database (Dere et al. 1997; Landi et al. 2013).

The error estimates shown in Table 1 ultimately derive from photon statistics errors, which are generally small due to the strength of the emission lines. As discussed earlier there is some uncertainty in the absolute calibration of EIS and this is not reflected in the intensity uncertainties. The lack of an absolute wavelength calibration for EIS means that there is a systematic uncertainty of $\approx 10 \text{ km s}^{-1}$ (see Sect. 4.3) that is not included in Table 1. The uncertainty in the non-thermal broadening is discussed in Sect. 4.4. The column emission measure is directly proportional to the line intensity, and so the uncertainty (not displayed in Table 1) can be obtained from the line intensity uncertainty.

The two coolest lines, O VI $\lambda 184.12$ and Fe X $\lambda 184.54$, were both fit with single Gaussians. The former is well-isolated in the spectrum, but the line’s doublet partner at 183.94 \AA is present at the edge of the window and masks out any high velocity ($200\text{--}300 \text{ km s}^{-1}$) component that may be present. However the partial line that is present is consistent with the expected $\lambda 183.94/\lambda 184.11$ intensity ratio, suggesting that there is no significant high velocity component.

Fe X $\lambda 184.54$ is blended on the short wavelength side with Fe XI $\lambda 184.41$, which is noticeably stronger (relative to $\lambda 184.54$) than in typical active region conditions, likely due to the high density of the brightening. The two lines were fit simultaneously with two Gaussians, and fits were found to be good, with in particular no suggestion that $\lambda 184.54$ is asymmetric.

The emission lines of Fe XII–XVI all show non-Gaussian profiles and they have been fit with multiple Gaussians. As EIS emission lines typically have a full-width at half-maximum of about 3 pixels then they are not ideally suited for detailed modeling in this manner. In particular, the parameters of weak components can be quite uncertain. For this work, we force the multiple Gaussian components for a single line to have the same width. While there is no physical justification for this, it does provide a baseline against which the plasma components of different ions can be compared and the results described later suggest that this is valid.

Fe XII $\lambda 192.39$ line is very close to the edge of its wavelength window and also lies on a sloping background level resulting from the nearby strong Fe XXIV $\lambda 192.03$ line. The line shows a clear asymmetry, with a steeper blue side to the profile, and has been fit with two Gaussians. The stronger $\lambda 195.12$ line also shows a clear asymmetry, but the profile is complicated by the presence of Fe XII $\lambda 195.18$ in the red wing. This line becomes quite strong at high densities (see, e.g., Young et al. 2009) and thus, if the two Gaussian model for $\lambda 192.39$ is assumed for $\lambda 195.12$ then $\lambda 195.18$ would enhance the component on the red side of the line. Fitting two Gaussians to the profile confirms that this is the case and, given the difficulties in deconvolving the blend we choose not to present the parameters for $\lambda 195.12$.

The density sensitive Fe XIV lines at 264.79 and 274.20 \AA are both blended: $\lambda 264.79$ with Fe XI $\lambda 264.77$, and $\lambda 274.20$ with Si VII $\lambda 274.18$. It is not possible to directly estimate the contributions of either of these lines to the Fe XIV lines from the flare spectra, however the authors have studied complete EIS spectra of an active region and find that the contributions are typically $< 5\%$ when the Fe XIV lines are strong. We therefore believe it is reasonable to neglect these blending species. Both Fe XIV lines show clear asymmetries such that the long wavelength sides of the profiles are less steep than the short wavelength sides. The $\lambda 274.20$ long wavelength wing extends beyond the edge of the wavelength window (which was only 16 pixels wide) and a two Gaussian fit with a constant background was used. We note that the $\lambda 274.20$ profile is very similar to that found by Doschek et al. (2012) during the rise phase of a M1.8 flare. The $\lambda 264.79$ wavelength window is wider than that for $\lambda 274.20$ but the long wavelength wing is still found to extend beyond the window edge, and a three Gaussian fit was performed with a constant background. The third, weakest Gaussian is at a velocity of $+166 \text{ km s}^{-1}$. There is a nearby Fe XVI line at 265.00 \AA which,

if it is assumed to have the same velocity as the dominant Fe xvi $\lambda 262.98$ component, would place it at $+180 \text{ km s}^{-1}$ in the Fe xiv $\lambda 264.79$ reference frame. The Fe xvi $\lambda 265.00/\lambda 262.98$ ratio has a fixed value of 0.096 based on atomic physics parameters, while the intensity ratio of the third Gaussian to the dominant intensity component of $\lambda 262.98$ is 0.16. We thus conclude that the third Gaussian component to Fe xiv $\lambda 264.79$ is dominated by Fe xvi and so we do not list it in Table 1. The two Gaussian fits to $\lambda 264.79$ and $\lambda 274.20$ lead to very similar LOS velocities and non-thermal velocities for the two components, giving confidence that the fits accurately model the line profiles. The intensity ratios of the two components are different, however, which reflects different densities for the two plasma components – this is discussed in Sect. 4.6.

Fe xv $\lambda 284.16$ shows a dominant intensity component with two weaker components either side and was fit with three Gaussians with the same width. $\lambda 284.16$ is known to be partly blended with Al ix $\lambda 284.03$, but this is negligible for the present spectrum ($\lambda 284.16$ is the strongest line by intensity of the lines measured).

Fe xvi $\lambda 262.98$ shows a similar line profile to Fe xv $\lambda 284.16$ with a dominant intensity component and weaker emission on each side. The short wavelength emission could not be accurately fit with a single Gaussian and so two Gaussians were necessary, giving four in all. A weak, unknown line is found in EIS spectra at 262.70 \AA (Brown et al. 2008), corresponding to a velocity of -320 km s^{-1} which is too far away to account for the Fe xvi component at -249 km s^{-1} . We note that Del Zanna et al. (2011) showed a Fe xvi $\lambda 262.98$ line profile for a flare kernel that also displayed an extended blue wing that was fit with two Gaussian components corresponding to upflow speeds of 60 and 170 km s^{-1} .

The Fe xxiii and Fe xxiv line profiles are the most striking in the flare kernel spectrum as they show strong blue-shifted emission at around -400 km s^{-1} in addition to a weaker component near the rest velocities of the lines (Figure 6). We note that the Fe xxiii $\lambda 263.77$ profile is quite similar to that shown by Watanabe et al. (2010) from a C9.7 flare kernel. The approximate background levels in the spectrum, as determined from the minimum intensity within each line’s wavelength window, are also shown in Figure 6. The narrowness of the wavelength windows used for the study means that the background levels are likely to be over-estimates of the real background.

The similarity of the line profiles for all three lines provides strong evidence that the highly-blueshifted components are real and not due to strong emission in emission lines on the short wavelength sides of each line, but we briefly discuss known blending issues for each.

Del Zanna et al. (2011) demonstrated that two weak lines blend with Fe xxiii $\lambda 263.77$ between -50 and -150 km s^{-1} (relative to $\lambda 263.77$). Figure 13 of their work also showed that there is another line at about -350 km s^{-1} that potentially could compromise the high velocity component found here. This line is found in quiet Sun and active region spectra (Brown et al. 2008), so it is probably formed at temperatures of $\log T = 6.0\text{--}6.2$. From an active region spectral atlas obtained on 2011 February 20, we find that Fe xii $\lambda 192.39$ is around a factor 170 times more intense than the line at 263.4 \AA . From Table 1, $\lambda 192.39$ is only a factor 3 stronger than the line at 263.4 \AA (interpreted

as the blue wing of $\lambda 263.77$) giving strong evidence that the strong blue-shifted component seen in Figure 6(a) is in fact due to Fe XXIII.

Several lines blend directly with Fe XXIV $\lambda 192.03$, but when the flare line becomes strong it easily overwhelms these lines. The blending lines are Fe VII $\lambda 192.01$, Fe VIII $\lambda 192.04$, Fe XI $\lambda 192.02$ and an unknown line at 192.09 \AA (Young & Landi 2009; Del Zanna 2009, 2010), and a useful guide to the extent of the blending can be made by considering the strength of the nearby Fe XII $\lambda 192.39$. The combined blending lines between 192.01 and 192.09 \AA can exceed the strength of the $\lambda 192.39$ line in some circumstances (Landi & Young 2009), but generally they are much weaker. It is not possible to estimate the extent of blending in the present spectra, but it is possible that they make a significant contribution to the rest component of the Fe XXIV. The width of the line is consistent with formation from a very hot ion, however. On the short wavelength side of the profile there is Fe XIV $\lambda 191.81$ which blends with the highly-blueshifted component of the Fe XXIV line. The CHIANTI Fe XIV model predicts that this line is about 2% of the strength of Fe XIV $\lambda 274.20$ and so based on the intensities in Table 1 this line can be shown to be negligible.

Fe XXIV $\lambda 255.11$ has several lines nearby, and the narrow width of the EIS observing window makes it difficult to fit the spectrum. The lines near to $\lambda 255.11$ are an unknown line at 254.70 \AA , Fe XVII $\lambda 254.86$, Fe VIII $\lambda 255.10$, Fe VIII $\lambda 255.37$ and Fe X $\lambda 255.39$. The Fe XVII line is particularly important when studying blue-shifted components of the Fe XXIV line as it becomes strong in flares and lies within the blue wing, however there is no evidence that the line is significant in the present spectrum, and so the observed spectral features are fit with two Gaussians to represent the rest and highly-blueshifted components of Fe XXIV $\lambda 255.11$. The similarity of the measured velocities to those of Fe XXIV $\lambda 192.03$ give confidence in the fit, although the non-thermal velocities are somewhat lower. This could be due to the fact that the background level is difficult to estimate due to the many blending lines.

We highlight here the fact that the Fe XXIV $\lambda 192.03/\lambda 255.11$ ratios for the two velocity components vary significantly from the value expected from atomic theory. The CHIANTI atomic model gives an expected ratio of 2.5, which is independent of density and only very slightly temperature dependent. The ratios found here are 3.9 and 6.2 for the blue-shifted and rest components, respectively. The rest component of $\lambda 192.03$ could be over-estimated because of the blending noted earlier, while the blending lines for $\lambda 255.11$ could also lead to over-estimation of this line’s components although we feel this is likely to be offset by an over-estimate of the spectrum background level.

To investigate the Fe XXIV ratio further, flare data from 2011 February 16 obtained after the flare peak were studied. At such times the Fe XXIV emission shows little dynamics (in terms of broadening or Doppler shifts) and is very strong so it should be free from blending. We found $\lambda 192.03/\lambda 255.11$ ratios ranging from 4.7 to 5.1 in six spectra, again significantly above the theoretical ratio. G. Del Zanna has suggested in several papers (Del Zanna & Ishikawa 2009; Del Zanna 2011, 2012) that there is a calibration problem for EIS whereby lines near 250 \AA are too weak

relative to lines in the EIS SW channel by a factor of up to two. The Fe XXIV results found here appear to confirm this.

4.3. Dynamics: Doppler shifts

The line-of-sight (LOS) velocities given in Table 1 are derived from Doppler shifts of the lines relative to “rest” wavelengths. There is no direct means to determine an absolute wavelength scale for EIS, and so indirect methods are needed – see Young et al. (2012) for a discussion. For the present work, we used the 10 Y-pixels at the bottom of the Fe XV $\lambda 284.16$ slit image to generate a pixel mask that represented a background region. The region at the bottom of the raster, while still dominated by active region plasma, is well-separated from the locations where the main flare dynamics occur, and thus is relatively stable. From these background spectra, the centroids of the following lines are measured: Fe X $\lambda 184.54$, Fe XII $\lambda\lambda 192.39, 195.12$, Fe XIV $\lambda\lambda 264.79, 274.20$, Fe XV $\lambda 284.16$ and Fe XVI $\lambda 262.98$, which are assumed to correspond to rest wavelengths. The rest wavelengths at the location of the flare kernel are then determined by simply applying the known EIS slit tilt values (Kamio et al. 2010). The remaining lines are either not present in the background spectra or are too weak to be measured reliably. These lines are paired with the nearest of the measured background lines, and the “rest separations” of the lines are assumed to be those determined from the rest wavelengths within the CHIANTI atomic database (Dere et al. 1997; Landi et al. 2013). This then allows the rest wavelengths of the lines not measured in the background spectra to be determined from those lines that are. This method of determining rest wavelengths is not as accurate as that described by Young et al. (2012), and we estimate an accuracy of $\pm 10 \text{ km s}^{-1}$. As can be seen from Table 1, however, velocities much larger than this are seen in the flare spectra.

Figure 7a shows the velocities derived for the EIS emission lines and their various components. The velocities are divided into five groups that we believe are physically connected. For example, the lines of Fe XII–XVI all show a weak red-shifted component and are represented by the light gray points. For the lines formed over $\log T = 5.5\text{--}6.5$, the velocities of the dominant emission components are represented by the blue points. The change from redshift to blueshift between Fe X and Fe XII is similar to the patterns found by Milligan & Dennis (2009) and Watanabe et al. (2010), which were cited as evidence of explosive evaporation. A dashed line connects the Fe XVI high velocity component to those of Fe XXIII and Fe XXIV to indicate that they might be related, although this is speculative.

The Fe XXIII and Fe XXIV lines both show a highly-blueshifted plasma component that is stronger than the plasma component that is close to the rest velocity, and the profiles are shown in Fig. 6. This result demonstrates that a *dominant*, high-velocity upflow component can be seen during flares when a spectrometer has high spatial resolution. As discussed in the introduction, earlier X-ray spectra averaged over the whole disk always revealed a dominant plasma component near the rest velocity of high temperature lines, with the high velocity component present as a weak

shoulder to this component. A previous observation of a dominant high velocity component in the Fe XXIII $\lambda 263.77$ line was presented by Watanabe et al. (2010) – see the middle panel of Figure 4 of their work – who found a velocity of -382 km s^{-1} from during the rise phase of a C9.7 flare. This suggests that such profiles may be typical of M-class flares, although the observation is sensitive to the timing and position of the EIS slit.

4.4. Dynamics: non-thermal line broadening

The measured widths of the EIS emission lines comprise three components: an instrumental width, a thermal width, and a non-thermal width. The instrumental width is known and varies with the positions of the spectra along the EIS slit (Young 2011). The thermal width is determined by assuming an isothermal temperature for the plasma emitting the particular ion species under consideration. For the present case we use the T_{mem} values given in Table 1. The non-thermal width is the remaining line width after the thermal and instrumental widths have been subtracted and is usually expressed as a velocity, ξ , defined as

$$4 \ln 2 \left(\frac{\lambda}{c} \right)^2 \xi^2 = W^2 - W_{\text{I}}^2 - W_{\text{th}}^2, \quad (1)$$

where λ is the wavelength of the emission line, c the speed of light, W is the full-width at half-maximum (FWHM) of the fitted Gaussian function, W_{I} is the instrumental width and W_{th} is the thermal width, both expressed as FWHM values. The uncertainties on ξ are determined from the $1\text{-}\sigma$ measurement errors on W and an estimated uncertainty of 3 m\AA on W_{I} (Young 2011).

The values of ξ are given in Table 1 and displayed graphically in Figure 7b. The blue points show the values derived from O VI through Fe XVI. As noted previously, the emission lines for Fe XII–Fe XVI were fit with multiple Gaussians forced to have the same width, and it is noticeable that a large decrease in ξ occurs between Fe X and Fe XII. We believe this is due to the fact that the Fe X line was fit with one Gaussian, while Fe XII was fit with two. The black, unfilled square in Figure 7b shows the non-thermal velocity if the Fe XII line is fit with a single Gaussian, giving a much higher value. This suggests that the large width of the Fe X line arises from multiple velocity components that are unresolved in the line profile.

The relatively small non-thermal velocities of Fe XII–XVI suggest that, when the background coronal emission is subtracted and individual plasma components can be identified through multiple Gaussian fits, then these components do not show any extra broadening over typical coronal plasma. Therefore enhanced broadening of coronal lines found in previous measurements is likely to be due to the superposition of multiple plasma components with different velocities rather than, say broadening due to turbulence.

The red and green points in Figure 7b show the ξ values for the fast upflowing and stationary components of the Fe XXIII and Fe XXIV lines (see also Figure 7a), and they are found to be very

similar at around 120 km s^{-1} . Milligan (2011) previously presented non-thermal velocity measurements from a flare kernel and found remarkably similar values to those found here, although in that case only an at-rest plasma component was detected.

4.5. Emission measure

The fourth quantity shown in Table 1 is the column emission measure, which is determined directly from the measured line intensity through the expression:

$$4\pi I = \frac{hc}{\lambda} \epsilon(X) C_\lambda EM(d) \quad (2)$$

where I is the measured line intensity, h Planck’s constant, c the speed of light, λ the wavelength of the emission line, $\epsilon(X)$ the element abundance of element X relative to hydrogen, C_λ contains various atomic parameters and $EM(d)$ is the column emission measure. The atomic parameters contained in C_λ are computed using the CHIANTI routine INTEGRAL_CALC, available in *Solarsoft*. The temperatures shown in Figure 7c are the temperatures of maximum emission, T_{mem} . The coronal abundances of Schmelz et al. (2012) have been used, the ionization balance calculations are those from CHIANTI (Dere et al. 2009), and a density of $3.4 \times 10^{10} \text{ cm}^{-3}$ was assumed (see Sect. 4.6). We note that the emission measure values are insensitive to the precise density used, however.

An additional emission measure point shown in Figure 7c was derived from the AIA 94 Å channel as follows. At temperatures of $\approx 10 \text{ MK}$, this channel is dominated by Fe XVIII $\lambda 93.93$ and so an emission measure can be derived by assuming that the plasma is isothermal at the $\log T_{\text{mem}} = 6.85$ value of this line. We compute an isothermal spectrum from CHIANTI for the A94 channel, convolve it with the A94 response function, and sum the result. The count rate per second in the A94 channel, C , (expressed as data numbers per second) can then be related to the column emission measure as

$$EM = 5.25 \times 10^{26} \alpha C, \quad (3)$$

where α accounts for the difference in spatial pixel size between AIA and EIS due to the fact that the flare kernels are not resolved by either instrument (see Sect. 5), and takes a value of 0.18. The isothermal spectrum used for this calculation was computed using the CHIANTI ionization balance, the hybrid coronal abundances of Schmelz et al. (2012), a density of $3 \times 10^{10} \text{ cm}^{-3}$, and unit column emission measure; the pre-flight A94 response function, available through the *Solarsoft* AIA_GET_RESPONSE routine, was used.

To determine the A94 count rate, the EIS-AIA co-alignment procedure (Sect. A) enabled the position of the EIS slit relative to AIA to be found. The region in the AIA image corresponding to the $2''$ wide EIS slit was extracted, the A94 counts summed over the brightening, and a background level subtracted, leaving a total count rate of $11,470 \text{ DN s}^{-1}$. The A94 emission measure is then

$6.02 \times 10^{30} \text{ cm}^{-5}$. Due to the method used we consider this an upper limit to the real emission measure.

Figure 7c shows the A94 emission measure point lies within a temperature gap in the EIS emission measure distribution, and thus provides valuable information. EIS does have access to Ca XVII $\lambda 192.86$ (formed at 6 MK) and unblended Fe XVII lines (formed at 4 MK), but these lines were not obtained in the present study.

Including the AIA point, the emission measure distribution is fairly uniform from 0.3 MK to 30 MK. The rest components of the hottest ions (green points in Figure 7c) have similar values to those derived from the dominant emission components of the cooler ions (blue points in Figure 7c). The fast upflowing hot plasma (red points) has an emission measure around a factor 2.5 larger than that for the rest components, and the A94 emission measure value is closer to this value, perhaps suggesting that Fe XVIII also has a dominant intensity component from the upflowing plasma. The redshifted components of Fe XII–XVI have significantly lower emission measures (gray points in Figure 7c), with a sharp drop between Fe XIV and Fe XV, while the fast upflowing component of Fe XVI is much stronger than that of Fe XV (light blue points).

All of the EIS emission lines used in the present study are from iron ions, except for O VI and we note that the choice of abundance file would affect the O VI emission measure value. If photospheric abundances had been used, then the O VI emission measure value would be reduced by a factor three relative to the iron values.

4.6. Density and emitting volume

Two density diagnostics are available from the HH_Flare_180x160_v2 study: Fe XII $\lambda 195.18/\lambda 195.12$ and Fe XIV $\lambda 264.79/\lambda 274.20$. The Fe XII lines can not be accurately separated due to the non-Gaussian profiles in the flare kernel, but the Fe XIV ratio is useful and has been applied in previous EIS analyses by, for example, Doschek et al. (2007), Milligan (2011) and Del Zanna et al. (2011).

Table 2 shows the electron number densities, N_e , derived from the Fe XIV line intensities given in Table 1 for the two plasma components. Component 1 has the stronger emission in both lines and has a velocity of $\approx -30 \text{ km s}^{-1}$, while component 2 has a velocity of $+65$ to $+70 \text{ km s}^{-1}$. Atomic data for the density diagnostic come from version 7.1 of the CHIANTI database (Landi et al. 2013).

The column depth, d , is an important parameter that can be derived from spectroscopic data as it can potentially yield smaller length scales than those obtained by directly imaging a plasma. For example, Del Zanna et al. (2011) found a column depth of 10 km for a flare kernel observed by EIS. Unfortunately the column depth also has large uncertainties associated with it due to the dependence on the square of the density – the uncertainties shown in Table 2 are derived by propagating the uncertainties on I and $\log N_e$. In addition, we cannot be certain of the absolute

iron abundance: the Schmelz et al. (2012) hybrid coronal abundance value³ of 7.85 lies between the Feldman et al. (1992) coronal value of 8.10 that is commonly used, and the photospheric value of 7.52 (Caffau et al. 2011), thus introducing an additional factor two uncertainty.

A further uncertainty lies in the EIS absolute calibration. Pre-launch, the uncertainty was considered to be 22% (Lang et al. 2006) but the degree to which the instrument sensitivity has degraded, and any wavelength sensitivity that this degradation has, are uncertain at the time of writing. As highlighted by the Fe XXIV $\lambda 192.03/\lambda 255.11$ ratio discussed earlier, a factor of two uncertainty is possible.

The values of d derived here may thus, at worst, be uncertain to a factor four, however the relative values of d between the two plasma components is much more accurate as the abundance and absolute calibration uncertainties do not apply. Implicit in the calculation of d is the assumption that the emission line intensities come from a region with cross-sectional area $2'' \times 1''$. If we assume instead that the emitting volume is a cube, then the side of this cube is $d_c = \sqrt[3]{2d}$ – a parameter that we refer to as the cubic column depth. We discuss the size of the emitting volume in more detail in the following section, where higher resolution AIA images are presented.

5. SDO data analysis

Figure 8 shows images of the flare kernel site obtained by the AIA instrument. The mid-point of the EIS exposure that produced the kernel spectrum discussed in the previous section was 07:40:16 UT and so the AIA images closest to this time were chosen. AIA has nine different EUV and UV filters, but four of these gave badly saturated images. Even for the images displayed, only A94 and A335 are not saturated at any location.

An important point to note is that the basic morphology of these images is very similar, and inspection of other data from the sequence of AIA images confirms that this is generally true. This is also consistent with the intensity images from EIS (Figures 3 and 4). We are thus confident that

³We use the standard abundance notation here whereby the abundance is expressed as $\log \epsilon(\text{Fe}) + 12$.

Table 2. Quantities derived from the Fe XIV $\lambda 264.79/\lambda 274.20$ ratio.

Plasma Component	Ratio	$\log (N_e/\text{cm}^{-3})$	d/arcsec	d_c/arcsec
1	2.44 ± 0.05	10.53 ± 0.05	4.77 ± 1.10	2.12
2	2.02 ± 0.14	10.15 ± 0.11	8.44 ± 4.30	2.57

the flare kernels emit over a continuous range of temperatures from the chromosphere (as observed through the 1600 and 1700 Å filters of AIA) through to temperatures of ≈ 30 MK (the Fe XXIV emission lines observed by EIS).

The yellow contours from the A94 image suggest that there are slight spatial offsets between the different AIA filters of up to 2 pixels. These are consistent with the expected accuracy of the AIA image alignments (R.A. Shine, private communication 2011), and so it is likely that the flare kernels are co-spatial at different temperatures.

The size of the flare kernels is very small and in fact the AIA de-spiking routine sometimes flags them as cosmic rays. For this reason it is necessary to use the `AIA_RESPIKE Solarsoft` routine to put flagged spikes back into the data. Two A94 intensity cross-sections are shown in the lower-right panel of Figure 8; one in the X-direction and one in the Y-direction. The column and row chosen for these cross-sections are indicated on the A94 image. The two different flare kernels shown have narrow, Gaussian shapes and by selecting a few such cross-sections we find average FWHMs of 2.2 and 2.0 pixels for the Y and X directions, respectively, with an uncertainty of about 0.10 pixels. These values are actually narrower than the AIA spatial resolutions of 2.5–3.0 pixels quoted in Boerner et al. (2012), suggesting the instrument is performing somewhat better than expected.

The twin vertical lines over-plotted on the A335 image of Figure 8 show the location of the EIS slit as determined from the co-alignment method described in Appendix A. It can be seen that EIS does not necessarily observe a single flare kernel, but instead a patch that may include two or more. This complicates interpretation of the column depth values d and d_c discussed in Sect. 4.6. The narrow intensity width across the line of flare kernels suggests an actual width significantly smaller than an AIA pixel. We can thus make a simple model whereby the emission is uniform along the line of kernels in the region observed by the EIS slit, and has a width across the kernel line of $0.3''$ (half of an AIA pixel). This would then imply the column depth of the kernel site is $d/0.3 = 16''$ from the EIS Fe XIV diagnostic. However, the appearance of the kernels in the AIA image should then be a series of “spikes”, unless the spikes are aligned along the observer’s line of sight. We conclude that the column depth derived from EIS is thus incompatible with the kernel sizes observed by AIA. The discrepancy could be resolved through one or more of the following: (i) the density is actually higher than derived from the Fe XIV ratio, (ii) the EIS sensitivity is higher than assumed at the wavelengths of the Fe XIV lines, and (iii) the abundance of iron is higher than assumed.

With the approximate position of the EIS slit established, it is possible to construct light curves for the kernel site observed by EIS in different AIA filters, and Figure 9 shows four such curves (the remaining AIA filters are affected by saturation). The light curves were derived by taking AIA images at the highest cadence (12 s for the EUV filters; 24 s for A1700) and extracting the spatial region corresponding to the $2'' \times 9''$ region that was used to create the EIS spectrum. The counts in this region were then summed. For Figure 9 the four light curves were normalized such that they each have the same pre-flare intensity and the same maximum intensity. It is clear that

all four channels brighten simultaneously (at least within the resolution of the AIA instrument), with the rise to maximum taking place in about 40 s from 07:39:00 to 07:39:40 UT. There is also a small intensity rise (a few percent) in all channels beginning at 07:38:00 UT which may be related to the following large increase. The EIS observation begins within 30 s of the kernel reaching its maximum intensity level.

A further light curve is shown in Figure 9 and was obtained from the X-Ray Telescope (XRT) on board *Hinode*. We have chosen data from the thin beryllium filter (Be-thin) which were obtained at about 30–45 s cadence over the period 07:35 to 07:41 UT. The observing mode changed after 07:41 UT, presumably because a flare mode was triggered, and Be-thin images were not obtained again until 07:50 UT. The flare kernels are prominent in the Be-thin images and Figure 10 compares the 07:40:14 UT image with the A94 image from 07:40:15 UT (see also Figure 8). The XRT image has been co-aligned with the A94 image using the brightenings in the middle-right of the images. Note that part of the XRT image is saturated. Based on the displayed co-alignment, the XRT light curve was extracted and normalized in the same manner as for the AIA images discussed earlier. The Be-thin filter has a peak temperature response at $\log T = 7.0$ (Golub et al. 2007) and confirms the high temperatures present in the flare kernel.

At this point we note that Brosius & Holman (2012) recently suggested that all of the AIA channels can brighten simultaneously in the early stages of a flare due to a large increase in emission at temperatures of 0.1–0.7 MK. This is evidenced by the fact that all of the AIA channels brightened simultaneously and several minutes before the hard X-ray bursts for a B5 microflare observed on 2010 July 21, in a manner consistent with previous observations of transition region emission lines observed with the SOHO/CDS instrument. The XRT light curve demonstrates that this is not the case in the present flare as the Be-thin filter has negligible sensitivity below $\log T = 6.0$ (Golub et al. 2007) while, in addition, the EIS emission measure plot of Figure 7c shows that the emission measure at $\log T = 5.5$ is not significantly larger than at other temperatures observed by EIS. The flare kernel studied here can thus not be explained as a transition region event.

6. Relation to magnetic field

Figure 11 shows where the flare kernels from the A94 07:40:15 UT exposure occur in relation to the LOS magnetic field and visible continuum intensity as measured from the HMI instrument. Alignment between the two instruments was checked by comparing images obtained $150''$ to solar-north and south of the region displayed in Figure 11. In such quiet Sun regions, small bright points in A1700 images generally correspond well with bright points seen in plots of the absolute LOS magnetic field strength. In the present case it was found that changing the A1700 image center by $(+0.3'', -0.5'')$ gave an improved alignment between the bright points for both quiet Sun pointings.

Now, comparisons of A1700 and A94 images of the flare kernels suggest that there is a spatial offset of $(0.0'', -0.8'')$ between the two, i.e., the A94 image needs to be moved to solar-north to

better match the A1700 image. Therefore the offset between A94 and the HMI LOS magnetograms is $(+0.3'', +0.3'')$. Given the assumptions made in this estimate, the accuracy may be as large as $\approx 1''$, however we can have some confidence that the brightenings are aligned along the ridge of positive magnetic polarity in Figure 11 (upper panel), rather than the narrow channel of weak opposite polarity just to the south of it, or the area of weak magnetic field to the north. Averaging a number of spatial pixels around the location of the flare kernel site considered in the present work yields an average line-of-sight magnetic field strength of 1030 ± 150 G. The comparison with the continuum intensity image (lower panel of Figure 11) shows that the brightenings lie within penumbra regions and extend towards, but not into, the sunspot umbra on the right side of Figure 11.

The HMI magnetograms are obtained at 45 s cadence and it is possible to search for changes in the signal between frames. Changes of up to 100 G are found at the location of one of the kernels between frames at 07:39:05 and 07:39:50 UT, and between 07:40:35 and 07:41:20 UT, however it is likely that such changes may simply represent plasma dynamics (velocity shift and/or line broadening) in the FeI line used for the magnetogram measurements rather than an actual magnetic field change, and so we choose not to identify them as magnetic field changes.

7. Discussion and summary

Active region AR 11458 produced a confined M1.1 class flare on 2011 February 16 that peaked at 07:44 UT. On one side of the active region a number of intense flare kernels were observed spectroscopically by the *Hinode*/EIS instrument between 07:40 and 07:41 UT. The present work focussed on one flare kernel site observed by EIS at 07:40:16 UT, and various spectroscopic parameters were measured. In addition, images from the SDO/AIA instrument were used to study temporal and spatial properties of the kernel site. We believe the analysis presented here gives the most complete set of ultraviolet observations yet obtained of flare kernels and present an important reference data-set against which other observations of these important energy release events can be compared. The key results are summarized below.

AIA and XRT images demonstrated that the flare kernel site reached maximum brightness in about 40 s, with a weak intensity enhancement for a minute immediately prior to this. Of the four AIA channels that were not saturated (spanning temperatures from the chromosphere to 10 MK) the intensity increase was simultaneous within the resolution limits of the AIA instrument. The flare kernel is one of several that lie along a line of length $\approx 25''$ that is found to align with a ridge of strong, positive magnetic field that is related to a nearby sunspot. The kernel is located in the penumbra of this sunspot where the magnetic field strength is ≈ 1000 G. The flare kernel sizes are at the resolution limit of the AIA instrument, suggesting sizes of $< 0.6''$ ($\lesssim 400$ km). In addition they have a similar morphology at all temperatures from the chromosphere to 30 MK, and are co-spatial to within the alignment uncertainties of the AIA channels.

A single EIS spectrum of the flare kernel was obtained about 30 s after the kernel reached maximum intensity, and the following properties were determined.

- The LOS velocities of the dominant emission components of lines from O VI to Fe XVI (0.3–2.5 MK) decrease monotonically from +35 km s^{−1} (downflows) at log $T = 5.5$ to −60 km s^{−1} (upflows) at log $T = 6.4$. The transition from downflows to upflows occurs around log $T = 6.1$.
- Fe XXIII and Fe XXIV lines (formed at 10–30 MK) show two plasma components, one at ≈ -400 km s^{−1}, and a weaker one at ≈ 0 km s^{−1}.
- Lines from Fe XII–XVI show two to four emission components. Each line has a red-shifted component at around +60 to +70 km s^{−1}, while Fe XV and Fe XVI have blue-shifted components at around −150 km s^{−1}. There is also evidence for a further Fe XVI component at −250 km s^{−1}.
- All lines show non-thermal velocity broadening, although for Fe XII–XVI – lines possessing multiple plasma components – the values are quite small at around 20–30 km s^{−1}. The cooler O VI and Fe X lines have larger broadenings of 60–80 km s^{−1}, perhaps reflecting unresolved plasma components. The hottest lines, Fe XXIII and Fe XXIV have large broadenings of around 100–120 km s^{−1}.
- Emission measure values derived from EIS are fairly uniform with temperature, with values of $3\text{--}10 \times 10^{29}$ cm^{−5}. The AIA 94 Å emission measure value fills a gap in the temperature coverage of EIS and is consistent with the EIS values.
- The dominant, blueshifted emission component of Fe XIV (2 MK) has a density of 3.4×10^{10} cm^{−3}; the weaker, redshifted component has a density of 1.4×10^{10} cm^{−3}. The column depths implied by these densities are significantly larger than the observed sizes of the flare kernels.

Prior to the availability of AIA and EIS, the limited spatial resolution of previous flare kernel observations prevented direct comparisons with theoretical models of the chromospheric evaporation process, and so one method for modeling the solar emission lines was to construct ensemble models of multiple events to match the data (Hori et al. 1997, 1998; Warren & Doschek 2005). The new data from AIA and *Hinode* presented here demonstrate that it is possible to obtain high quality data of individual kernel sites. Many 1D models of the evaporation process have been performed previously and we briefly consider the model of Allred et al. (2005), which is a development of the earlier work of Fisher et al. (1985), Hawley & Fisher (1994) and Abbett & Hawley (1999).

Firstly, the observation of upflowing plasma at 400 km s^{−1} is clear evidence for explosive evaporation and by comparing with the light curves from XRT and AIA we can say that chromospheric evaporation was underway 80 s after line intensities began their large increase, and about 30 s after

the intensities reached their peak value. For comparison, the models of Allred et al. (2005) showed that explosive evaporation began 73 s and 1 s after the start of events with heat fluxes of 10^{10} and 10^{11} erg cm $^{-2}$ s $^{-1}$, respectively. The time taken to reach maximum intensity is around 80 s and 2 s (based on Figure 15 of Allred et al. 2005) for these two cases compared to the observed rise of 40 s. We speculate that the rise time observed from AIA data may serve as a proxy for the heat flux, and thus the heat flux for the present flare kernel may be between 10^{10} and 10^{11} erg cm $^{-2}$ s $^{-1}$.

The small size of the flare kernels as seen by AIA suggest scales of $< 0.6''$ ($\lesssim 0.4$ Mm) at all temperatures. The 1D models of Allred et al. (2005) were computed over heights of 0 to 10 Mm, with chromospheric lines formed over 0–1.5 Mm, and coronal lines over 1–10 Mm. Taking into account density, the coronal emission is likely concentrated over 1–3 Mm regions. The observations are thus not inconsistent with the models. The high densities measured from the EIS Fe XIV diagnostic are consistent with the later phases of the Allred et al. (2005) models when dense chromospheric plasma has been heated to coronal temperatures.

Allred et al. (2005) focussed on the modeling of chromospheric emission lines, and so comparisons with the higher temperature EIS velocities are not possible. We note that the measurement of multiple emission components of the lines from Fe XII to Fe XVI, together with the large line widths of other lines, suggest that there are several flow patterns within the flare kernel, which may simply imply that there are multiple loop footpoints within the kernel that are not resolved by EIS. If this is the case, though, then there is some coherence between how these footpoints behave as evidenced by distinct velocity features in the line profiles.

Finally, the emission measure results show fairly uniform emission over the temperature range 0.3–30 MK, which constrains the heating profile for upper transition region and coronal plasma.

The similarity of the flare kernel results presented here with those of Watanabe et al. (2010) for a similar size flare, and also to aspects of the results from Milligan & Dennis (2009), Milligan (2011), Del Zanna et al. (2011) and Doschek et al. (2012), suggests that flare kernels may exhibit consistent properties. A survey of such events with EIS and AIA would thus be extremely valuable. RHESSI observations are extremely important too as they can constrain the energy input to the flare kernel site.

This work was funded by NASA under a contract to the U.S. Naval Research Laboratory. Hinode is a Japanese mission developed and launched by ISAS/JAXA, with NAOJ as domestic partner and NASA and STFC (UK) as international partners. It is operated by these agencies in co-operation with ESA and NSC (Norway).

Facilities: Hinode(EIS), Hinode(XRT), SDO(AIA), SDO(HMI), GOES.

A. Co-aligning EIS and AIA

The EIS and AIA data were spatially coaligned by constructing a pseudo raster image from the AIA 335 Å filter images and comparing with the EIS raster image obtained in the Fe XVI $\lambda 262.98$ line. The A335 filter is dominated by Fe XVI $\lambda 335.40$ and Fe XVI $\lambda 262.98$ is a strong, clean line in the EIS raster.

Figure 3 shows that the flare kernels appeared as compact brightenings in five adjacent EIS exposures, and the alignment was performed by trying to reproduce the intensity ratios of these five brightenings in the A335 pseudo raster image. The A335 images nearest in time to each of the EIS exposures were identified and for each data columns were extracted corresponding to the expected position of the EIS slit. The EIS slit width is $2''$, spanning more than three AIA pixels, and partial intensity columns were considered where necessary to ensure that exactly $2''$ strips were extracted. The solar-X positions of the EIS slit were obtained through IDL procedures, and were assumed to have an offset from the real solar-X positions.

The A335 intensity corresponding to each of the EIS brightenings is obtained by summing 15 pixels on each side of the intensity maximum in the simulated intensity column. By adjusting the EIS–AIA offset we attempted to reproduce the intensity ratios of the five EIS brightenings. Simply by inspecting the ratios by eye the appropriate X-offset could be established to be between +11 and +12 arcsec. The final value of +11.7 arcsec was determined by performing a least-squares analysis.

Figure 12 (left panel) shows the A335 pseudo raster image derived with this method using the 11.7 arcsec offset. This can be compared to the actual EIS image in the right panel (this image was derived by fitting the $\lambda 262.98$ emission line with a Gaussian at each spatial pixel). In the middle panel the AIA image has been convolved with a Gaussian of FWHM 3.5 arcsec in the Y-direction, to better match the spatial resolution of EIS. It can be seen that the correspondence between the AIA and EIS images is very good, giving confidence that the co-alignment for the brightenings is accurate.

One should caution that the EIS exposure times are significantly longer than those of AIA (8 s vs. 2.9 s), and there is not a one-to-one correspondence between EIS and AIA exposures. For such dynamic events as the flare brightenings this leads to a significant source of uncertainty in the alignment method presented here, but the results suggest that an accuracy of 1 arcsec is not unreasonable.

REFERENCES

- Abbett, W. P., & Hawley, S. L. 1999, *ApJ*, 521, 906
- Allred, J. C., Hawley, S. L., Abbett, W. P., & Carlsson, M. 2005, *ApJ*, 630, 573
- Antonucci, E., et al. 1982, *Sol. Phys.*, 78, 107

- Benz, A. O. 2008, *Living Reviews in Solar Physics*, 5
- Boerner, P., et al. 2012, *Sol. Phys.*, 275, 41
- Brosius, J. W. 2003, *ApJ*, 586, 1417
- Brosius, J. W. 2013, *ApJ*, 762, 133
- Brosius, J. W., & Holman, G. D. 2012, *A&A*, 540, A24
- Brosius, J. W., & Phillips, K. J. H. 2004, *ApJ*, 613, 580
- Brown, C. M., Feldman, U., Seely, J. F., Korendyke, C. M., & Hara, H. 2008, *ApJS*, 176, 511
- Caffau, E., Ludwig, H.-G., Steffen, M., Freytag, B., & Bonifacio, P. 2011, *Sol. Phys.*, 268, 255
- Cheng, C.-C., Oran, E. S., Doschek, G. A., Boris, J. P., & Mariska, J. T. 1983, *ApJ*, 265, 1090
- Culhane, J. L., et al. 2007, *Sol. Phys.*, 243, 19
- Del Zanna, G. 2009, *A&A*, 508, 513
- Del Zanna, G. 2010, *A&A*, 514, A41
- Del Zanna, G. 2011, *A&A*, 533, A12
- Del Zanna, G. 2012, *A&A*, 537, A38
- Del Zanna, G., Berlicki, A., Schmieder, B., & Mason, H. E. 2006, *Sol. Phys.*, 234, 95
- Del Zanna, G., & Ishikawa, Y. 2009, *A&A*, 508, 1517
- Del Zanna, G., Mitra-Kraev, U., Bradshaw, S. J., Mason, H. E., & Asai, A. 2011, *A&A*, 526, A1
- Dere, K. P., Landi, E., Mason, H. E., Monsignori Fossi, B. C., & Young, P. R. 1997, *A&AS*, 125, 149
- Dere, K. P., Landi, E., Young, P. R., Del Zanna, G., Landini, M., & Mason, H. E. 2009, *A&A*, 498, 915
- Doschek, G. A., Feldman, U., Kreplin, R. W., & Cohen, L. 1980, *ApJ*, 239, 725
- Doschek, G. A., Mariska, J. T., Warren, H. P., Culhane, L., Watanabe, T., Young, P. R., Mason, H. E., & Dere, K. P. 2007, *PASJ*, 59, 707
- Doschek, G. A., Warren, H. P., & Young, P. R. 2012, *ApJ*, submitted
- Feldman, U., Mandelbaum, P., Seely, J. F., Doschek, G. A., & Gursky, H. 1992, *ApJS*, 81, 387
- Fisher, G. H., Canfield, R. C., & McClymont, A. N. 1985, *ApJ*, 289, 414

- Fludra, A., Bentley, R. D., Lemen, J. R., Jakimiec, J., & Sylwester, J. 1989, *ApJ*, 344, 991
- Golub, L., et al. 2007, *Sol. Phys.*, 243, 63
- Graham, D. R., Fletcher, L., & Hannah, I. G. 2011, *A&A*, 532, A27
- Harra, L. K., Démoulin, P., Mandrini, C. H., Matthews, S. A., van Driel-Gesztelyi, L., Culhane, J. L., & Fletcher, L. 2005, *A&A*, 438, 1099
- Harra, L. K., Sterling, A. C., Gömöry, P., & Veronig, A. 2011, *ApJ*, 737, L4
- Hawley, S. L., & Fisher, G. H. 1994, *ApJ*, 426, 387
- Hori, K., Yokoyama, T., Kosugi, T., & Shibata, K. 1997, *ApJ*, 489, 426
- Hori, K., Yokoyama, T., Kosugi, T., & Shibata, K. 1998, *ApJ*, 500, 492
- Kamio, S., Hara, H., Watanabe, T., Fredvik, T., & Hansteen, V. H. 2010, *Sol. Phys.*, 266, 209
- Kosovichev, A. G. 2011, *ApJ*, 734, L15
- Landi, E., & Young, P. R. 2009, *ApJ*, 706, 1
- Landi, E., Young, P. R., Dere, K. P., Del Zanna, G., & Mason, H. E. 2013, *ApJ*, 763, 86
- Lang, J., et al. 2006, *Appl. Opt.*, 45, 8689
- Lemen, J. R., et al. 2012, *Sol. Phys.*, 275, 17
- Mariska, J. T., & Muglach, K. 2010, *ApJ*, 713, 573
- Mason, H. E., Shine, R. A., Gurman, J. B., & Harrison, R. A. 1986, *ApJ*, 309, 435
- Milligan, R. O. 2011, *ApJ*, 740, 70
- Milligan, R. O., & Dennis, B. R. 2009, *ApJ*, 699, 968
- Milligan, R. O., Gallagher, P. T., Mathioudakis, M., Bloomfield, D. S., Keenan, F. P., & Schwartz, R. A. 2006a, *ApJ*, 638, L117
- Milligan, R. O., Gallagher, P. T., Mathioudakis, M., & Keenan, F. P. 2006b, *ApJ*, 642, L169
- Scherrer, P. H., et al. 2012, *Sol. Phys.*, 275, 207
- Schmelz, J. T., Reames, D. V., von Steiger, R., & Basu, S. 2012, *ApJ*, 755, 33
- Schrijver, C. J., Aulanier, G., Title, A. M., Pariat, E., & Delannée, C. 2011, *ApJ*, 738, 167
- Teriaca, L., Falchi, A., Cauzzi, G., Falciani, R., Smaldone, L. A., & Andretta, V. 2003, *ApJ*, 588, 596

- Teriaca, L., Falchi, A., Falciani, R., Cauzzi, G., & Maltagliati, L. 2006, *A&A*, 455, 1123
- Veronig, A. M., Gomory, P., Kienreich, I. W., Muhr, N., Vrsnak, B., Temmer, M., & Warren, H. P. 2011, *ApJ*, 743, L10
- Warren, H. P., & Doschek, G. A. 2005, *ApJ*, 618, L157
- Watanabe, T., Hara, H., Sterling, A. C., & Harra, L. K. 2010, *ApJ*, 719, 213
- Young, P. R. 2010, EIS Software Note No. 13, ver. 4
- Young, P. R. 2011, EIS Software Note No. 7, ver. 1
- Young, P. R., & Landi, E. 2009, *ApJ*, 707, 173
- Young, P. R., O’Dwyer, B., & Mason, H. E. 2012, *ApJ*, 744, 14
- Young, P. R., Watanabe, T., Hara, H., & Mariska, J. T. 2009, *A&A*, 495, 587

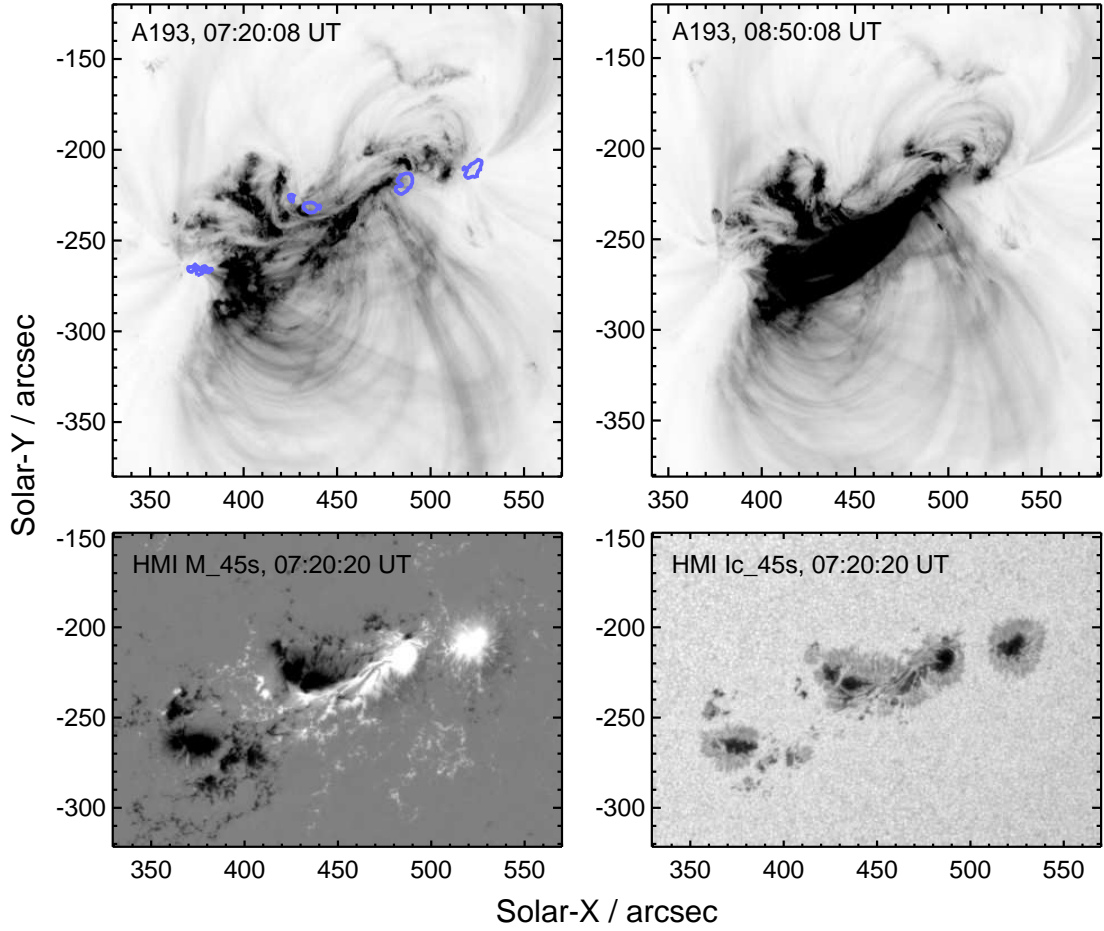


Fig. 1.— The upper panels show AIA 193 Å images obtained before and after the 2011 February 16 07:44 UT flare. A reverse intensity scaling has been applied and the maximum intensity value is 2500 DN s^{-1} in both images. The lower panels show HMI LOS magnetogram (left) and white light continuum (right) images from before the flare. The blue contours on the top-left image show the locations of the sunspot umbrae.

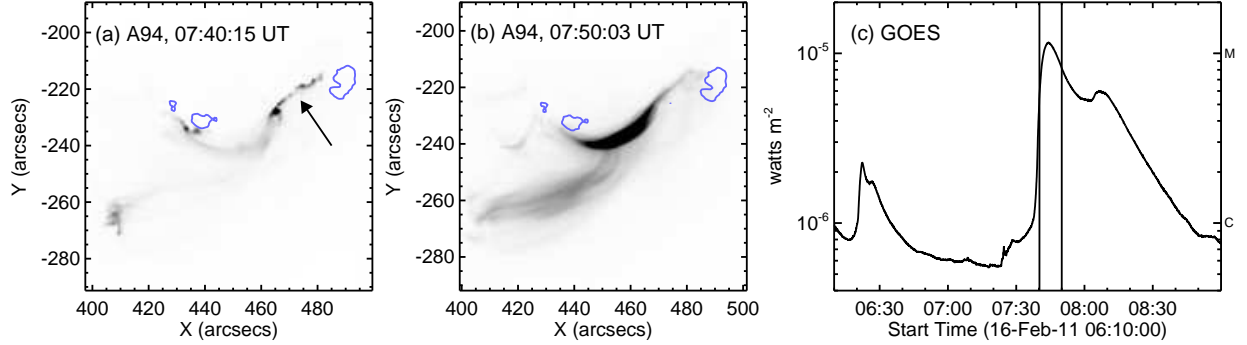


Fig. 2.— Panels a and b show AR 11458 at two different times, as seen in the AIA 94 Å filter. A negative intensity scaling is used, with black corresponding to the brightest regions. Both images have been saturated to a level of 3000 DN s⁻¹; the actual intensity maxima are 5301 and 5328 DN s⁻¹. An arrow indicates a group of flare kernels, one of which is studied in the present work. Blue contours show the location of sunspot umbrae as determined from co-temporal HMI data. Panel c shows the GOES 1–8 Å light curve, with two vertical lines representing the times at which the A94 images were obtained.

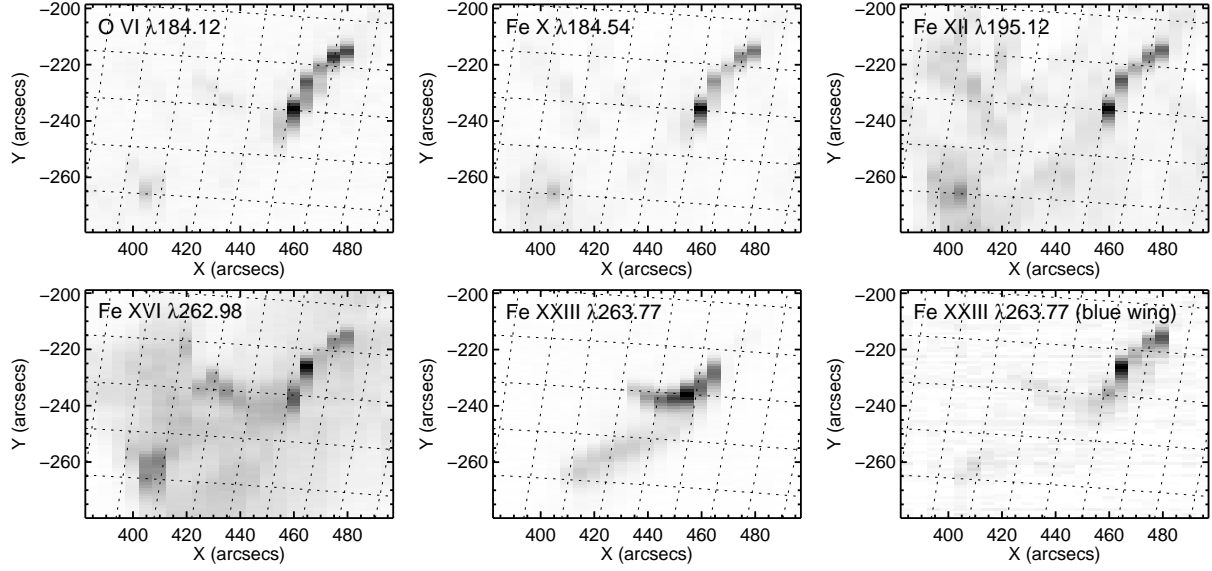


Fig. 3.— Six images from the EIS raster that began at 07:38:36 UT. A reverse intensity scaling has been applied to each image. The grid on each image shows lines of latitude and longitude, spaced at 1° intervals. The leftmost line of longitude is +24°, and the lowermost line of latitude is -22°. The Fe XXIII λ263.77 blue wing corresponds to Fe XXIII upflow velocities of around 350 km s⁻¹. See main text for more details.

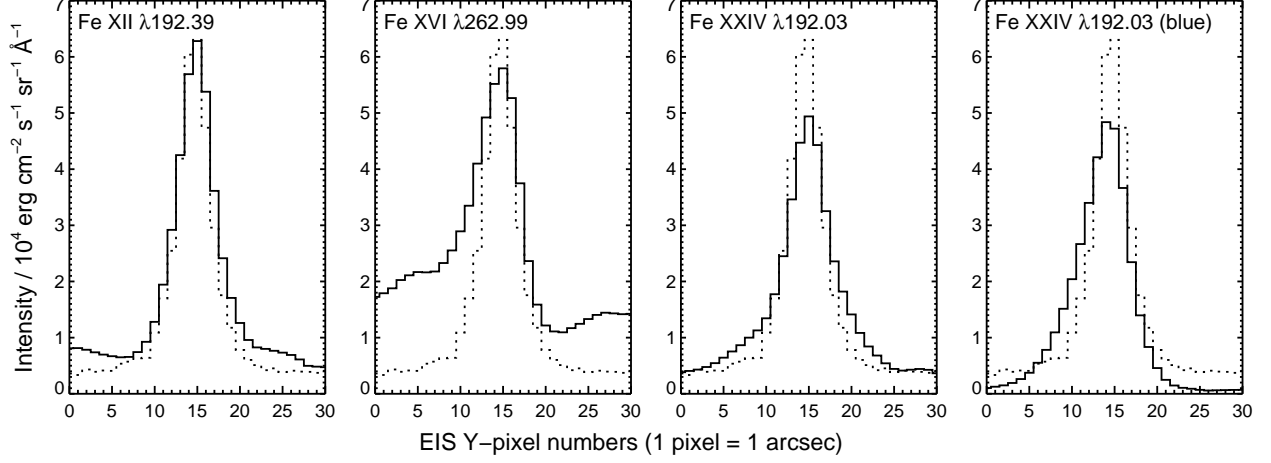


Fig. 4.— The dotted lines in each plot show the intensity cross-section of O VI $\lambda 184.11$. The solid lines show the intensity cross-sections of the four species identified in the top-left corner of each plot. The Fe XXIV $\lambda 192.03$ (blue) intensity was obtained at a wavelength of 191.77 Å , corresponding to a $\lambda 192.03$ velocity of -400 km s^{-1} . The intensity of the $\lambda 192.03$ (blue) cross-section has been divided by a factor 2. No scaling has been applied to the other cross-sections.

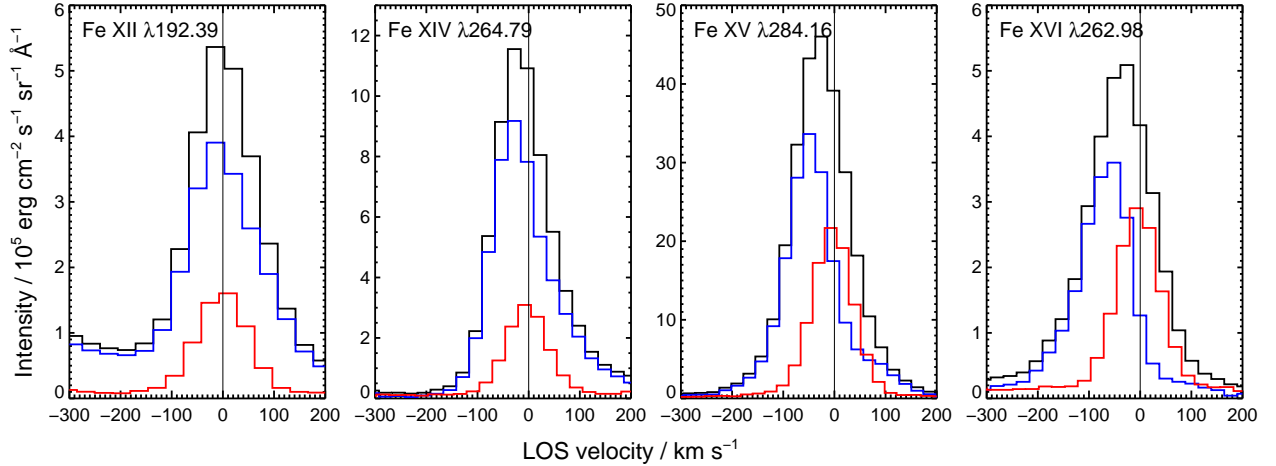


Fig. 5.— Four emission lines observed by EIS are shown. The red lines show the pre-flare spectrum, the black lines the flare kernel spectrum, and the blue lines the spectrum obtained by subtracting the pre-flare spectrum from the flare spectrum.

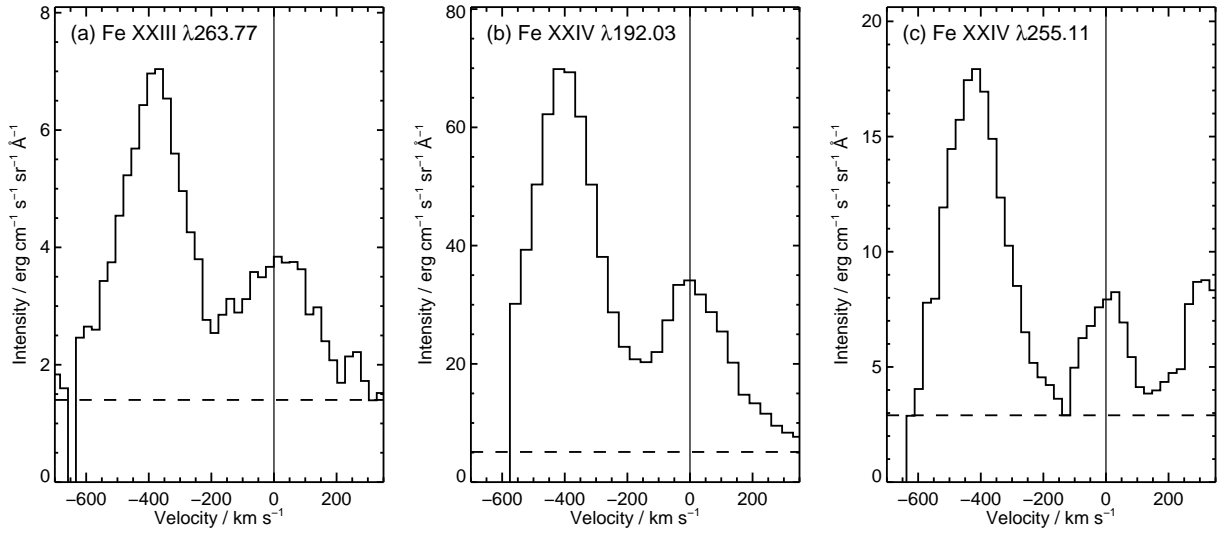


Fig. 6.— Emission line profiles from the flare kernel spectrum for (a) Fe XXIII λ 263.77, (b) Fe XXIV λ 192.03, and (c) Fe XXIV λ 255.11. The dashed lines indicate the background level in the spectra.

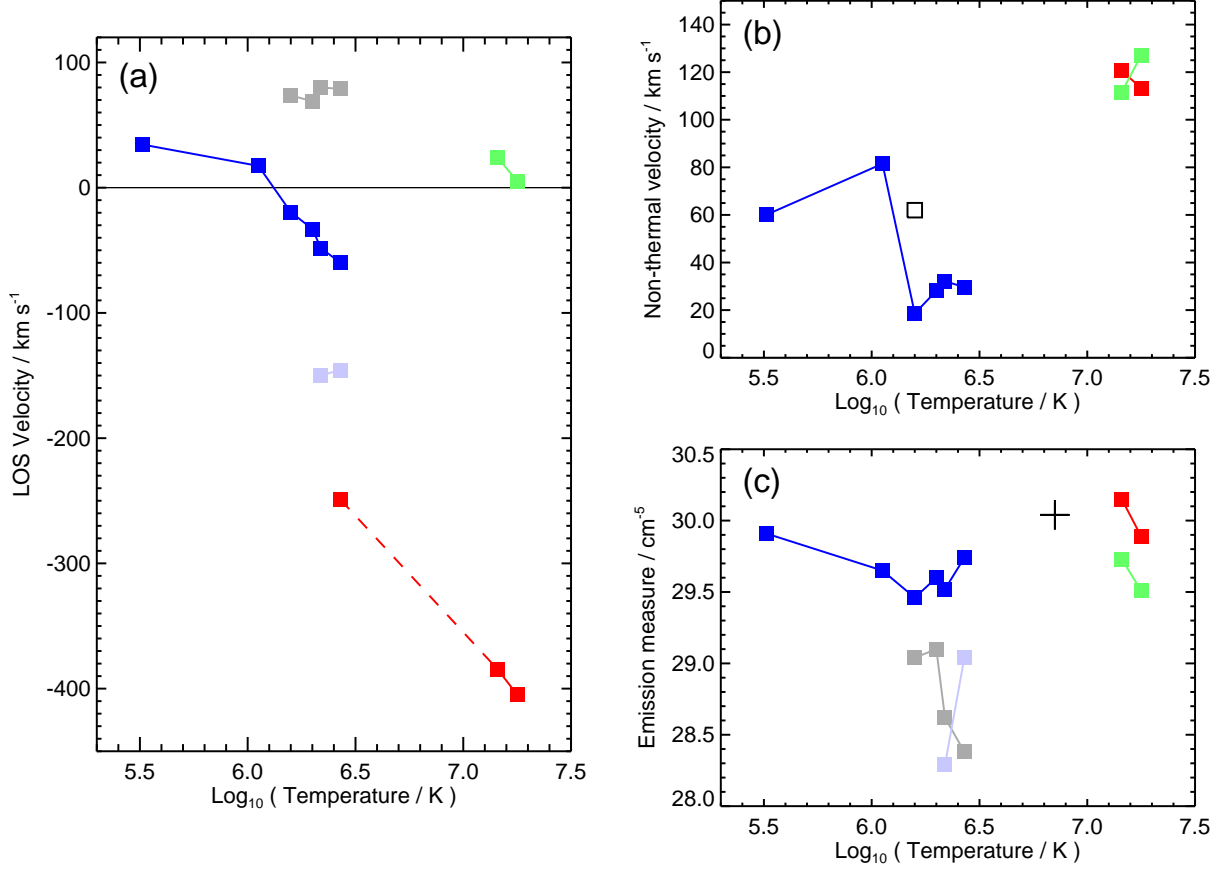


Fig. 7.— Plots showing (a) LOS velocity, (b) non-thermal velocity and (c) emission measure values derived from the EIS spectrum of the flare kernel. The colors of the points plotted in (b) and (c) correspond to the groups of velocity components shown in plot (a). Grey and light blue points are not shown on plot (b) as they have the same values as the set of blue points. The unfilled square in plot (b) shows the non-thermal velocity derived from Fe XII $\lambda 192.39$ when it is fit with a single Gaussian. The cross on plot (c) shows the value derived from the AIA 94 Å channel.

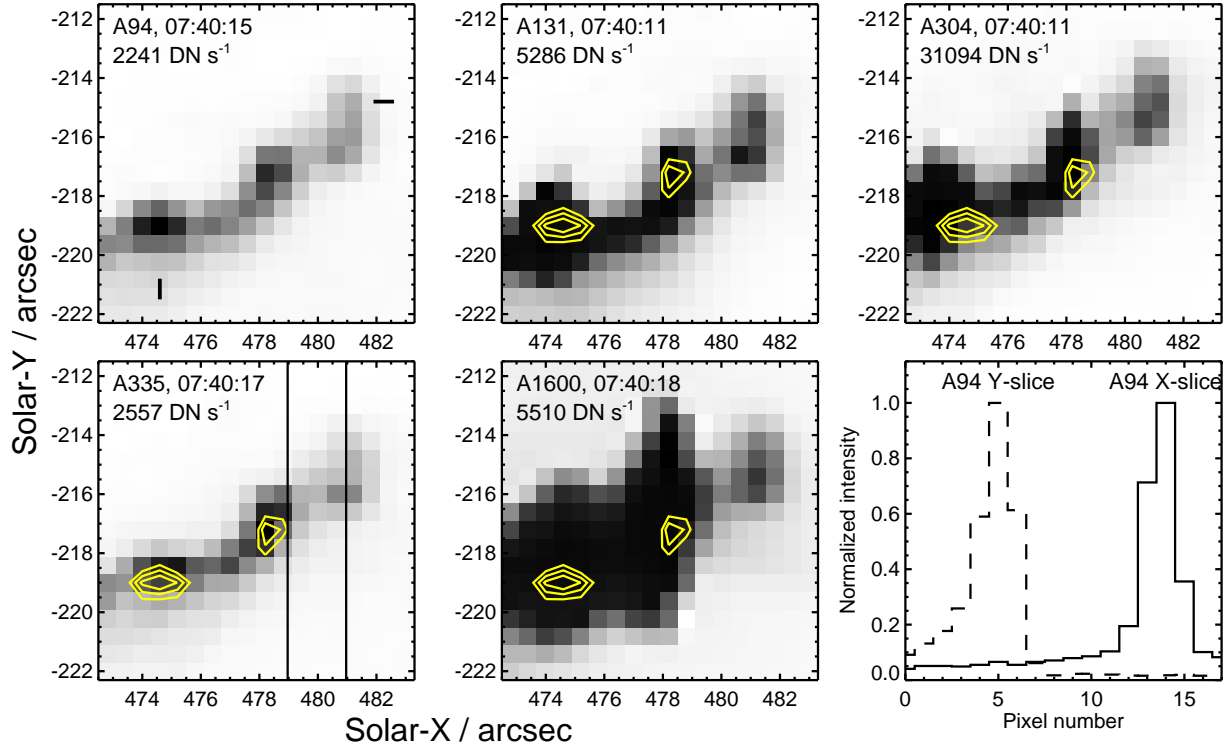


Fig. 8.— The top three panels, and two lower-left panels show AIA images of the flare kernel site at times ranging from 07:40:11 to 07:40:18 UT. The intensity scale is reversed such that dark areas correspond to high intensity. For each image the count rate of the brightest pixel in the image is displayed in the top-left. The yellow contours show the areas of highest intensity from the A94 image. The two vertical lines on the A335 image show the position of the EIS slit as determined from the co-alignment method. The two short, thick lines in the A94 image indicate the X and Y pixels used to create the intensity cross-sections plotted in the bottom-right panel.

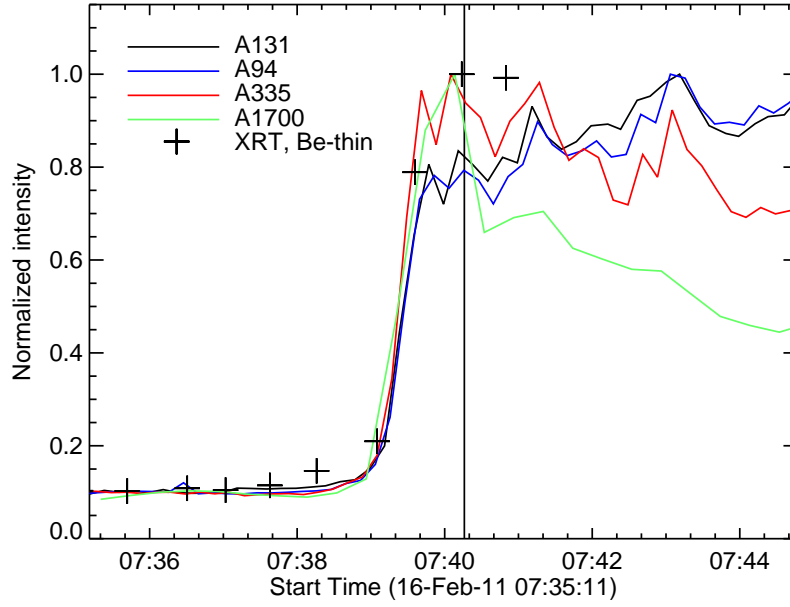


Fig. 9.— AIA light curves for the EIS flare kernel. Each curve has been normalized such that the median of the values before 07:38 is set to 0.1 and the maximum of the curve is set to 1.0. The vertical line denotes the midpoint time of the EIS exposure. A XRT light curve derived from the Be-thin filter is over-plotted with crosses.

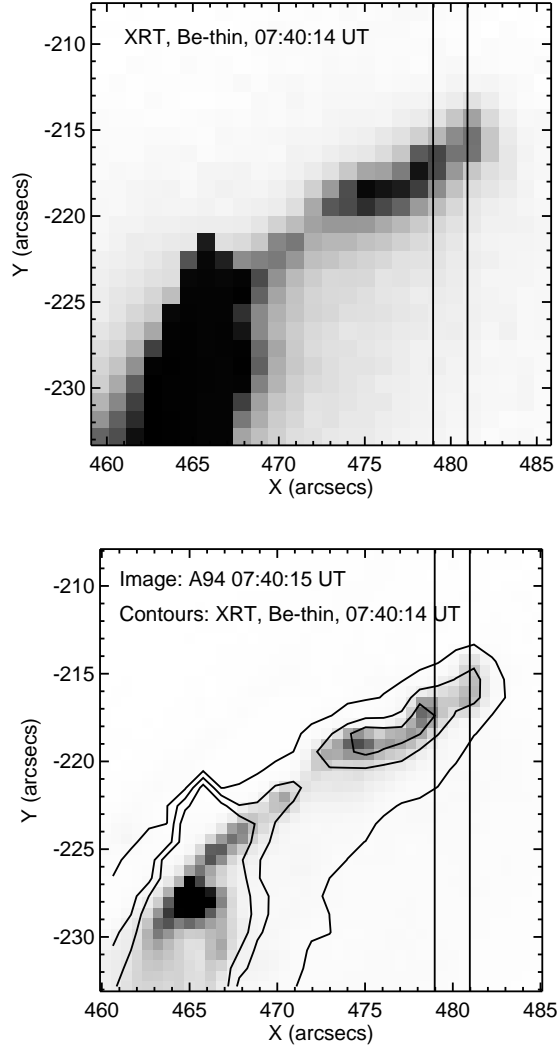


Fig. 10.— The upper panel shows an XRT image of the flare brightenings obtained at 07:40:14 UT with the thin beryllium filter. The lower panel shows the A94 image from 07:40:15 UT. The twin vertical lines show the location of the EIS slit at 07:40:16 UT. The contours on the lower panel show the XRT emission.

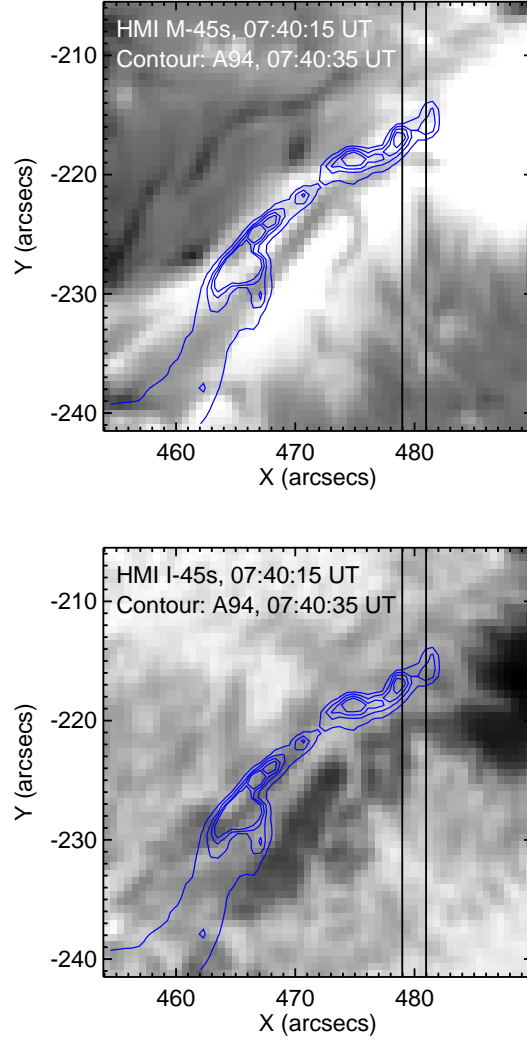


Fig. 11.— The upper panel shows a HMI LOS magnetogram, and the lower panel a HMI white light continuum image. The blue lines show intensity contours from the AIA 94 Å image. The parallel vertical lines indicate the position of the EIS slit at 07:40:16 UT.

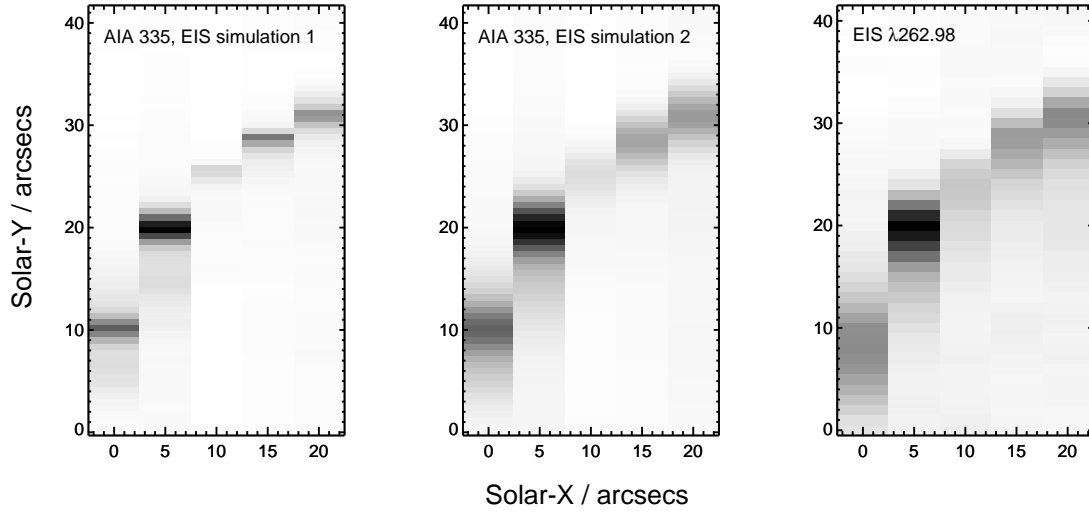


Fig. 12.— Images of the set of five flare brightenings observed by EIS between 07:40 and 07:41 UT. The left image is derived from A335 exposures, where data columns have been summed to match the 2 arcsec width of the EIS slit. The middle panel is derived from the left panel image by convolving the data in the Y-direction with a Gaussian of FWHM equal to 3.5 arcsec. The right panel shows the EIS Fe XVI λ 262.98 intensity image. Note that the displayed pixels have a width of 5 arcsec because the EIS raster used jumps of 5 arcsec between exposures.